



An experimental study of the gas entrapment process in closed-end microchannels

Ana V. Pesse, Gopinath R. Warriar *, Vijay K. Dhir

Mechanical and Aerospace Engineering Department, Henri Samueli School of Engineering and Applied Science, University of California, Los Angeles, CA 90095-1597, United States

Received 24 May 2005; received in revised form 30 July 2005
Available online 28 September 2005

Abstract

The physical mechanisms of the gas entrapment process in closed-end microchannels were investigated. Deionized water was the test fluid. The test pieces consisted of micromachined silicon squares with glass bonded on top. The microchannels had widths varying from 50 to 5 μm and had a mouth angle of 90° . Experiments show two main filling behaviors: (1) A single meniscus at the entrance, (2) Two or more menisci: one at the entrance and the other near the closed end. A single meniscus typically forms for higher contact angles ($\phi > 50^\circ$), while two or more menisci form for lower contact angles ($\phi \leq 30^\circ$). For $30^\circ \leq \phi \leq 50^\circ$, one or two interfaces were observed. In all cases, after sufficient time (hours to days), the microchannel was completely flooded. In general, increasing the depth and/or width increases the time taken to fill. On the other hand, decreasing the contact angle decreases the time taken to fill. Comparison of experimental data with predictions based on a simple mass diffusion model shows reasonable agreement.

© 2005 Elsevier Ltd. All rights reserved.

Keywords: Microchannel; Gas entrapment; Flooding

1. Introduction

During boiling, vapor bubble formation starts from microscopic nucleation sites on the heated surface. These nucleating cavities have trapped gas or vapor inside. The ability of a liquid to penetrate into these microscopic cavities depends on such factors as the contact angle (ϕ) of the liquid and the size and shape of the cavity. However, once the liquid penetrates into the cavity, it can either entrap the gas/vapor present in the cavity or floods the cavity entirely.

Bankoff [1] was the first to propose a quantitative criterion for gas entrapment in a wedge by an advancing liquid front. The critical parameters affecting the gas/vapor entrapment in such a cavity were the contact angle and the wedge angle. Conical cavities were approximated as wedge-shaped grooves. According to his criterion, a wedge-shaped cavity on a surface will trap vapor/gas when the contact angle is greater than the wedge angle.

Wang and Dhir [2] studied the effect of surface wettability on the active nucleation site density during pool boiling of water. In their work, they related the cavities that were present on a surface to those that actually became active. Based on the measured shape and size of the cavities present on the heater surface, they found that most of the deep cavities present on the surface were

* Corresponding author. Tel.: +1 310 825 9617; fax: +1 310 206 4830.

E-mail address: gwarriar@ucla.edu (G.R. Warriar).

Nomenclature

A	interfacial area	w	cavity mouth width
b	microchannel breadth	x_i	mole fraction of species i
c	molar concentration	X	position of the liquid–air interface inside the cavity
C_{He}	Henry constant	<i>Greek symbols</i>	
D_h	hydraulic diameter	ΔF	change in Helmholtz free energy
D_{12}	binary diffusion coefficient for chemical species 1 and 2	ρ	density
He	Henry number	σ	surface tension
J	diffusive mass flux	ϕ	contact angle
L_0	depth of microchannel	ψ_m	cavity mouth angle
M	molecular weight	<i>Subscripts</i>	
n_0	initial number of moles of air	air	air
P	pressure	i	species i
P_0	pressure of air	int	interface
R	radius of meniscus	liq	liquid
\mathfrak{R}	universal gas constant	u	liquid phase
r_c	cavity mouth radius	s	gas phase
T	temperature		
V	volume		

spherical in nature. Although a large number of conical cavities were present in the surface, these cavities were very shallow, which according to Bankoff's criterion were not expected to nucleate. It was found that as the wettability of the surface improves, the number density of cavities that actually nucleate decreases. Wang and Dhir [3] also evaluated the change in the Helmholtz free energy (ΔF) of a liquid droplet placed at the mouth of a cavity, with the free surface of the droplet exposed to gas or vapor. The equilibrium position of the interface was calculated by varying the location of the liquid–gas interface.

For a spherical cavity with mouth angle (ψ_m) of 30° they showed that for contact angles smaller than the cavity mouth angle (i.e., $\phi < \psi_m$), the free energy decreases as the interface moves to the bottom of the cavity. For these contact angles no gas will be trapped. However, for higher contact angles ($\phi > \psi_m$), the relative free energy reaches a minimum at $\alpha_s = 180^\circ - \phi$ and then increases to a maximum value at $\theta_s = 90^\circ - \phi$, where θ_s is the angular coordinate. Beyond $\theta_s = 90^\circ - \phi$, the free energy decreases. This suggests that the interface will move from its position above the cavity to the location where ΔF is minimum and will hence entrap gas in the cavity. Based on their analysis, the condition for entrapment of gas could be stated as,

$$\phi > \psi_{\min} \quad (1)$$

where ψ_{\min} is the minimum cavity side angle. The experimental results clearly showed that all the cavities that entrapped gas and were hence active nucleation sites

satisfied the condition given by Eq. (1). It should be noted that the model of Wang and Dhir was a quasi-static model, which did not consider diffusion of gas into the liquid. A similar analysis was done by Warriar [4] for a cylindrical cavity. For spherical, conical, and cylindrical cavities, $\psi_{\min} = \psi_m$.

Once a cavity entraps gas, increasing the temperature of the cavity or the liquid may result in an increase in the vaporization at the liquid–gas interface. According to Carey [5], the degree to which the entrapped gas helps vaporization depends on the rate at which the entrapped gas diffuses into the liquid and is carried away from the interface. Thus, once all the entrapped gas has diffused into the liquid, the cavity will be flooded.

Washburn [6] derived an equation to describe the spontaneous motion of a liquid–gas interface in an open ended capillary. His equation was based on the balance between the capillary force, the gravity force and the viscous force given by Poiseuille [7]. Since the inertial forces were neglected, the Washburn equation predicts an infinitely high initial velocity for the liquid during the early stages of interface advancement. It was Szekely et al. [8] who removed this discontinuity by applying the correct momentum balance for the entry flow. However since these studies were for open-end capillaries, they did not consider the effect of the gas entrapped within the capillary.

Yang et al. [9] measured the marching velocity of capillary menisci in microchannels (2 mm long). In the analytical model developed, the velocity profile was assumed to be parabolic and the pressure difference

across the liquid–gas interface was calculated using the “Laplace pressure drop”. Neglecting the acceleration term, they found that the position of the interfaces was proportional to the square root of time. In general, their experiments showed that filling time increases with increasing cross-sectional area of the microchannels. However, there is no mention as to whether the microchannels had an open or closed end. Also, no information is given regarding the filling mechanisms involved or the role of mass diffusion.

Akselrud and Altshuler [10] proposed that the degree to which the entrapped gas diffuses into the liquid significantly affects the nature of filling of a closed-end capillary. Dovgyallo et al. [11] observed the phenomenon of bilateral filling of conical capillaries with a closed end. They experimentally studied the filling of closed-end capillaries, with lengths varying from 30 to 1000 μm and radii from 0.4 to 15 μm with various liquids. They found that in a number of cases, the capillary is filled not only from the open end, but also from the closed end. However, for experiments with cylindrical capillaries, they found that the capillaries are filled only from the open end. In the conical capillaries, the closed end had a smaller cross-sectional area. This difference between cylindrical and conical capillaries was associated with the presence of two menisci of different curvatures in the conical case. They theorized that the second meniscus forms at the closed end of the capillary due to condensation from the liquid vaporized from the surface of the meniscus with lower curvature. They also found that, in the case of cylindrical capillaries, the rate at which air dissolves into the liquid was considerably lower than that for the conical capillaries.

Wang [12] performed a few experiments to observe the filling of water and methanol in glass capillary tubes closed at one end. The length of the capillary tubes was about 2 mm while the inner diameter varied from 10 to 40 μm . His results showed that as the capillary diameter increases the sorption rate increases. Additionally, it was found that the sorption rate for methanol (lower contact angle) was about three or four times larger than that for water (higher contact angle).

Migun and Azuni [13] carried out experiments using larger conical capillaries than those considered by Dovgyallo et al. They observed the same double side filling phenomena. In capillaries of radius, $R \geq 50 \mu\text{m}$ they also observed individual liquid droplets on the channel walls.

From the above discussion it is clear that for a given cavity size (and shape) liquids with certain contact angles will entrap gas in the cavity. Though the important parameters that affect the dynamics of the interface and subsequent entrapment of gas appear to be the liquid contact angle, cavity size, cavity shape, and liquid properties such as surface tension and viscosity, no quantitative information is available regarding the effects of each

of these parameters. Additionally, no quantitative information is available regarding the effects of gas diffusion on the dynamics of the interface and the gas entrapment process.

The objective of this study is to develop a basic understanding of the dynamics of liquid–gas interfaces in cavities and the process by which gas can be entrapped in these cavities. This experimental work will focus on the effects of the following parameters: cavity geometry (depth, mouth width, and mouth angle), as well as the static contact angle of the test liquid. Also of interest is the effect of gas diffusion on the interface dynamics and gas entrapment process.

2. Experimental apparatus

The purpose of the experiments was to set up a representation of a nucleation site or cavity to study the physical mechanisms of the gas entrapment process. In order to allow observation of the moving liquid interface in the cavity, closed-end microchannels with rectangular cross-sections were fabricated on a silicon substrate and covered with glass. The experimental setup consisted of a computer with image capturing software, a CCD camera, a microscope and the test pieces (Fig. 1).

Microchannels were fabricated with four entrance widths (5, 15, 30 and 50 μm) and three depths (50, 150 and 500 μm). The breadth (dimension going into the plane of the pictures) was about the same as the width and varied from 7 to 42 μm . Fig. 2(a) shows the schematic of a typical cavity and a simulated cavity.

The test samples were fabricated on 100 mm silicon wafers, using standard micromachining techniques. The samples were etched to the required depth and then diced into $2 \times 2 \text{ cm}$ pieces. Borofloat glass was then anodically bonded to these samples. Fig. 2(b) shows

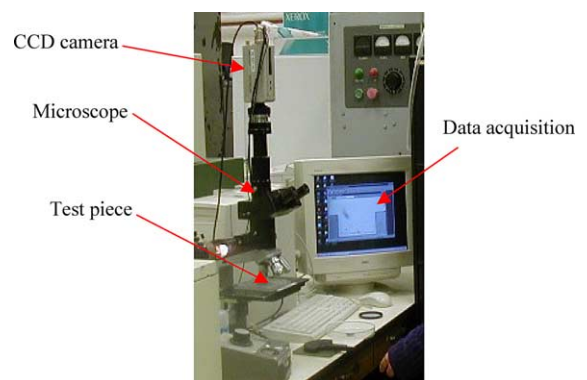


Fig. 1. Experimental setup.

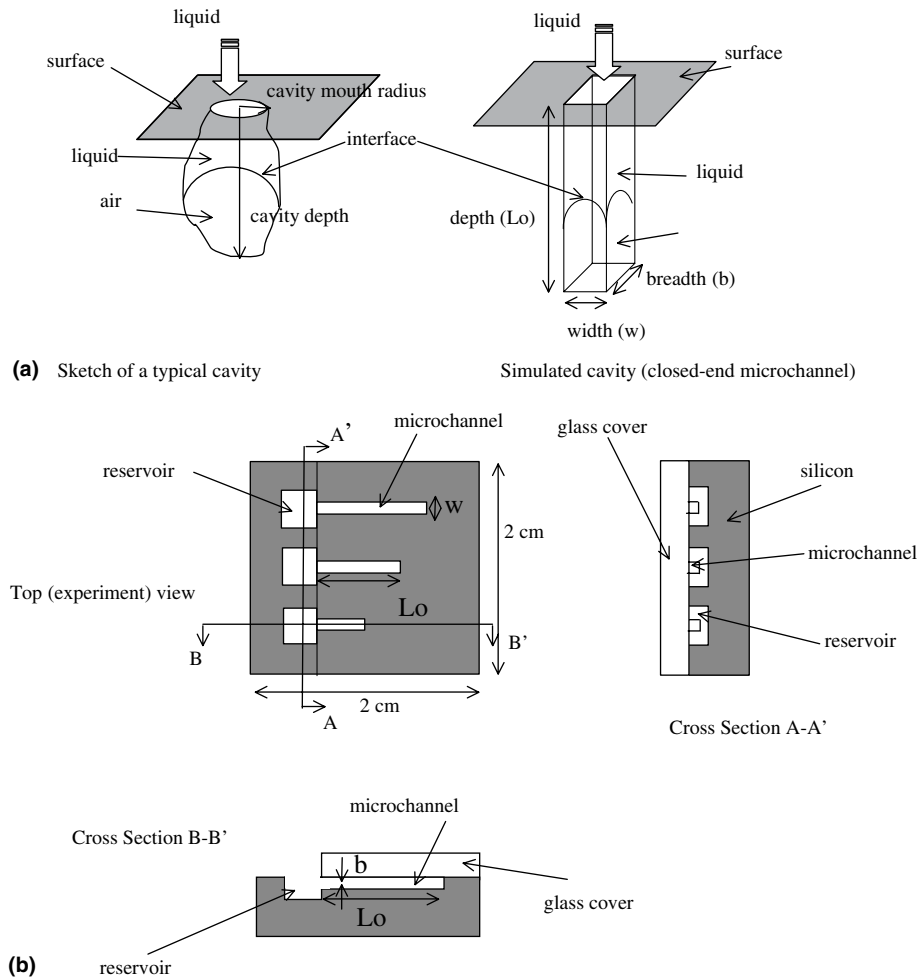


Fig. 2. Schematic of (a) an actual cavity and a simulated cavity and (b) test sample.

the schematic of the test samples. Each test sample had three to four microchannels on it with the open end (entrance of the microchannel) connected to a reservoir of square cross-section with side 1 mm and depth of around 300 μm . Further details can be found in [14].

3. Experimental procedure

The first experimental run for each test piece was conducted without any further surface cleaning, assuming that the microchannel remained clean during the anodic bonding process. The anodic bonding process subjects the test pieces to temperatures of around 300 $^{\circ}\text{C}$ for 2 h.

Before starting each experimental run, the contact angle between the liquid droplet and the silicon surface

was measured, so as to quantify the condition of the silicon surface inside the cavity. Since it was not possible to place a droplet in the microchannel, a small drop of the test fluid was placed in the reservoir using a syringe and a photograph was taken. The contact angle was measured from this photograph. Fig. 3 shows a typical photograph of a droplet in the reservoir and the contact angle measured.

After the first use of a test piece, it was thoroughly cleaned using a combination of the following processes: (1) Piranha bath (1:4, $\text{H}_2\text{SO}_4:\text{H}_2\text{O}_2$) at room temperature for 50 min, followed rinsing with DI water rinse, blow drying with nitrogen and then to dehydrate, baking at 110 $^{\circ}\text{C}$ for 40 min. (2) Supercritical Dryer, with CO_2 and pure methanol for 1 h. (3) Bake at 160 $^{\circ}\text{C}$ for 90 min by placing the sample on a hot plate. The purpose of the surface cleaning was to modify the contact angle of the test fluid in contact with silicon. The contact

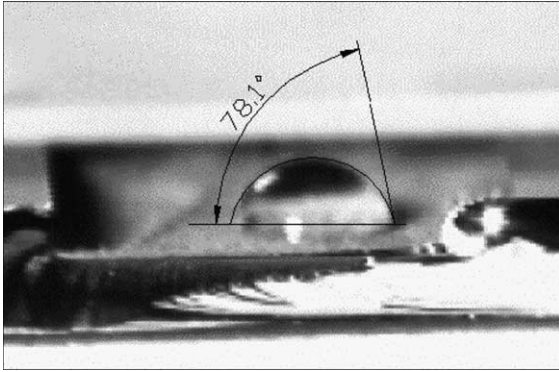


Fig. 3. Photograph of a liquid droplet in the reservoir.

angles corresponding to the cleaning procedures given above are listed as follows:

- After anodic bonding (before first use of new piece): $\phi \sim 60^\circ$.
- Used piece after Piranha bath (includes rinsing and dehydration bake): $\phi \leq 15^\circ$.
- Used piece after Piranha bath followed by supercritical dryer: $\phi \sim 0^\circ$.
- Same as (b) followed by hot bake at 160°C for 40 minutes: $\phi \leq 25^\circ$.

The contact angles corresponding to the cleaning procedures (b), (c), and (d), were obtained from the shape of the meniscus inside the microchannel. This method was adopted since it was very difficult to determine the contact angle by placing a droplet in the reservoir (due to the low contact angle, the droplet wets the surface). Table 1 gives the range of contact angles measured on the various test pieces.

Once the contact angle was recorded, the test piece was placed under a microscope equipped with a CCD camera. The test liquid was then placed in the reservoir and the entire filling process was recorded. Both the liquid and test sample were at room temperature (about 23°C). At the beginning (first 20 images) of the experiments an image was captured every 10 s and afterwards every 30, 60 and 120 s depending on the test liquid, contact angle and microchannel geometry.

Table 1
Dimensions and contact angles for various test pieces

Width [μm]	Cavity depth, L_0 [μm]		
	500	150	50
$w = 9, b = 5$	$12^\circ \leq \phi \leq 64^\circ$	$8^\circ \leq \phi \leq 55^\circ$	$8^\circ \leq \phi \leq 54^\circ$
$w = 19, b = 15$	$8^\circ \leq \phi \leq 62^\circ$	$15^\circ \leq \phi \leq 48^\circ$	$8^\circ \leq \phi \leq 37^\circ$
$w = 38, b = 24$	$8^\circ \leq \phi \leq 66^\circ$	$8^\circ \leq \phi \leq 90^\circ$	$23^\circ \leq \phi \leq 90^\circ$
$w = 56, b = 42$	$8^\circ \leq \phi \leq 67^\circ$	$8^\circ \leq \phi \leq 54^\circ$	$12^\circ \leq \phi \leq 90^\circ$

4. Data reduction

Once a sequence of images was recorded, it was necessary to measure the distance from the entrance of the cavity to the liquid–air interface. A Matlab program was used to read each image as a two-dimensional array of color values and determine the location of the liquid–air interface. The results were given in pixels (Fig. 4(a)), which are then converted to microns. Once the liquid had penetrated the microchannel, the contact angle inside the microchannel was measured from the shape of the meniscus. This was considered to be the actual static contact angle. Since two or more surfaces were in contact with the liquid, a mean value was calculated for the static contact angle. This angle was measured by analyzing the digital image with AutoCAD (Fig. 4(b)).

5. Measurement uncertainty

In these experiments only three quantities were measured: position of the liquid–air interface, time, and contact angle of the liquid in the microchannel. The position of the interface was measured in pixels and which was then converted to microns using a conversion factor that had its own uncertainty. The error in the pixel count was ± 2 pixels which correspond to an error of $\pm 5 \mu\text{m}$ in the measured microchannel depth. Thus the conversion factor uncertainty was 2%, 6%, and 20% for the 500 μm , 150 μm , and 50 μm long channels, respectively. The error associated with the measurement of the position of the interface was ± 4 pixels. Hence the overall error associated with the position of the interface was $\pm 10 \mu\text{m}$. The uncertainty of temporal measurements is 10 s, which is given by the frame rate of the camera. The uncertainty for the contact angles measured in the reser-

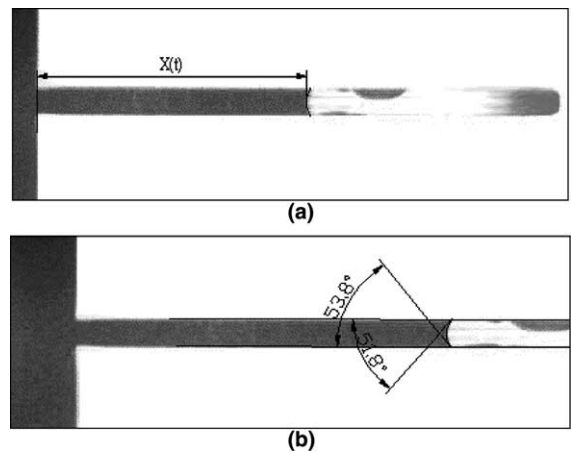


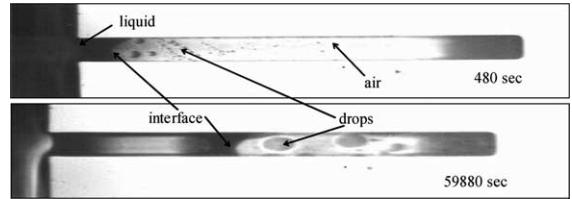
Fig. 4. Measurement of (a) interface position and (b) contact angle inside the microchannel.

voir of the test samples was estimated to be $\pm 5^\circ$, whereas the contact angles measured inside the microchannel had an uncertainty of $\pm 8^\circ$.

6. Results and discussion

In most of the experiments performed, only one liquid–air interface (moving from left to right, i.e., open end to closed end) was observed. Fig. 5(a) shows a sequence of photographs of the single liquid–air interface, while Fig. 5(b) shows the corresponding plot of the interface location as a function of time. From Fig. 5(b) it can be seen that the motion of the liquid–air interface is not smooth. The interface moves, remains stationary and then moves again. However, close to the closed end of the microchannel, the interface moves quite rapidly. It must be mentioned that in the ordinate in the plots does not begin at zero because the first photograph was typically taken after a time interval of 10 s.

A variation of this filling behavior (i.e. only one interface) occurs when in addition of the single interface, liquid droplets are also present on the channel walls as shown in Fig. 6(a). It can be seen that the initial droplets



(a)

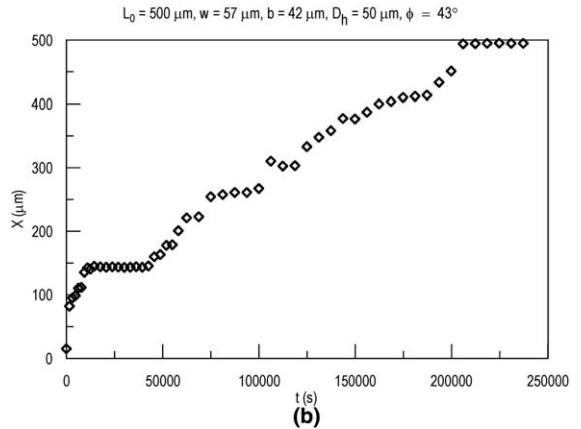
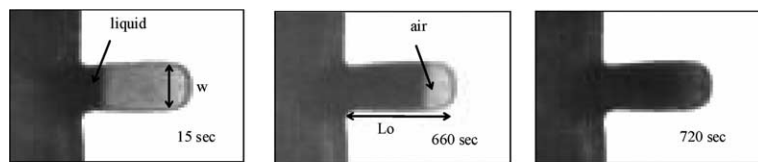


Fig. 6. Front advancing interface with droplets.



(a)

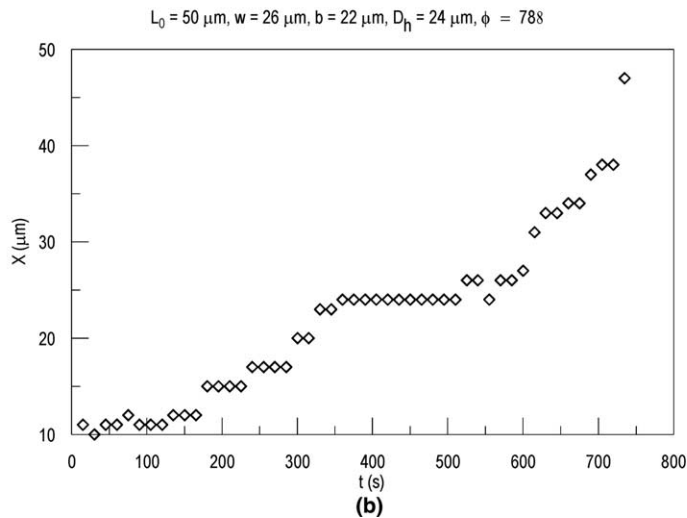


Fig. 5. Front advancing interface.

merge to form larger droplets and sometimes even merge with the advancing interface, which causes sudden jumps in the interface location. These sudden jumps are clearly seen in Fig. 6(b).

For experiments with low contact angles, a second mechanism by which the microchannel can be filled was observed. For these cases, two interfaces were observed; one at the entrance of the microchannel and the other at the closed end. Referring to the sequence of photographs shown in Fig. 7(a), initially only one interface is present but after 52,390 s a second interface appears near the closed end of the microchannel and starts moving towards the entrance, finally meeting up with the front interface and thus filling the microchannel. In most of the cases, when two interfaces were present, a thin film of liquid on the walls of the channel connected the two menisci. Fig. 7(b) shows the corresponding interface locations as a function of time.

A variation of this second mechanism was also observed. In these cases, in addition to the two menisci, liquid droplets were also present. This can be seen in Fig. 8(a). The film connecting the two menisci can also be clearly seen. The droplets on the walls of the channel grew and merged with each other and with the menisci. Fig. 8(b) shows a plot of the location of the interfaces as a function of time.

Additionally, in some instances, usually for longer channels, more than two interfaces were seen. This generally happens as a result of droplets growing and merging to fill up the channel and forming an interface. This is the case shown in Fig. 9(a), which starts with only one

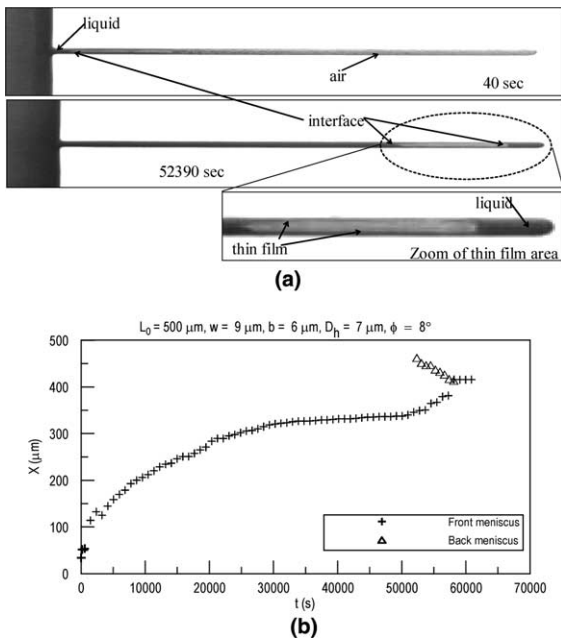


Fig. 7. Front and back advancing interfaces, with thin film.

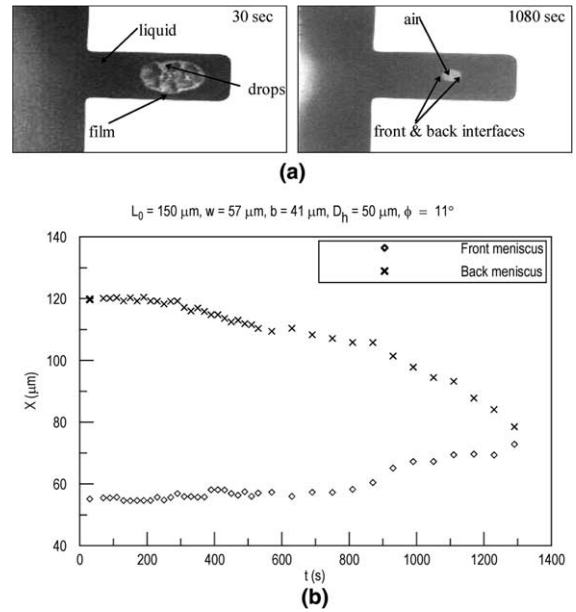


Fig. 8. Front and back advancing interfaces, with thin film and droplets.

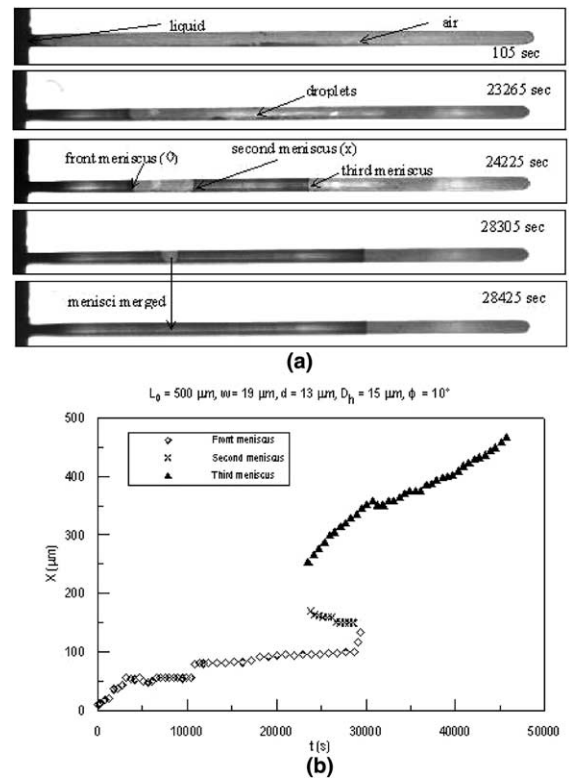


Fig. 9. Front, middle, and back advancing interfaces.

interface but after 23,385 s the liquid flowing along the side walls feeds the droplets present in the middle of

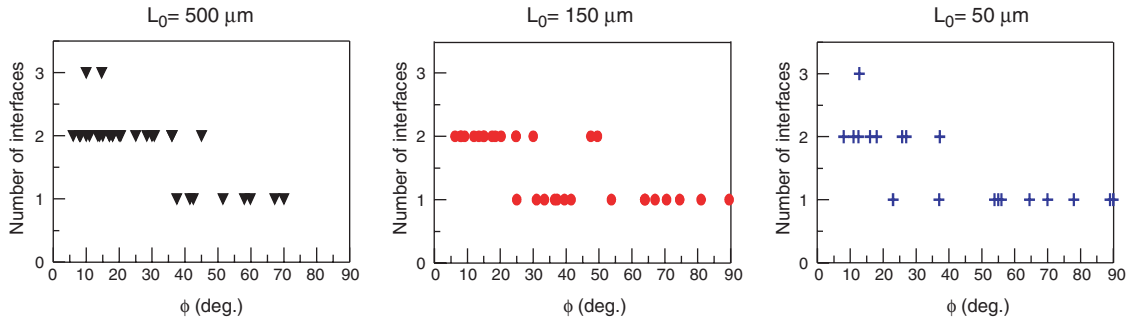


Fig. 10. Number of interfaces observed as a function of contact angle.

the channel with enough liquid to grow and merge forming two new interfaces. One of these interfaces moves towards the closed end of the microchannel while the other advances towards the first interface located closer to the entrance of the channel. Later, at 28,425 s, the middle interface that was moving towards the entrance merges with the original front interface. The described behavior can be seen clearly in Fig. 9(b), which shows the position of the interfaces as a function of time. There are three distinct stages: one corresponding to the original front interface (until 23,385 s), the second is the creation of the second and third interfaces, and finally the merging

of two interfaces (at 28,425 s) leaving only one interface closer to the end of the channel.

The experiments conducted, indicate that for $\phi \leq 30^\circ$, two interfaces connected by a thin liquid film were always observed. On the contrary, for $\phi > 50^\circ$, only one interface was observed. In the range between 30° and 50° both, one or two interfaces were observed. This is shown in Fig. 10 for different microchannels depths. Occasionally, for low contact angles ($\phi < 15^\circ$), three interfaces were also observed.

All the microchannels with rectangular cross-sections tested in this study were completely flooded given sufficient time. The time taken to completely flood the microchannel varied from seconds, to minutes, to hours to even days.

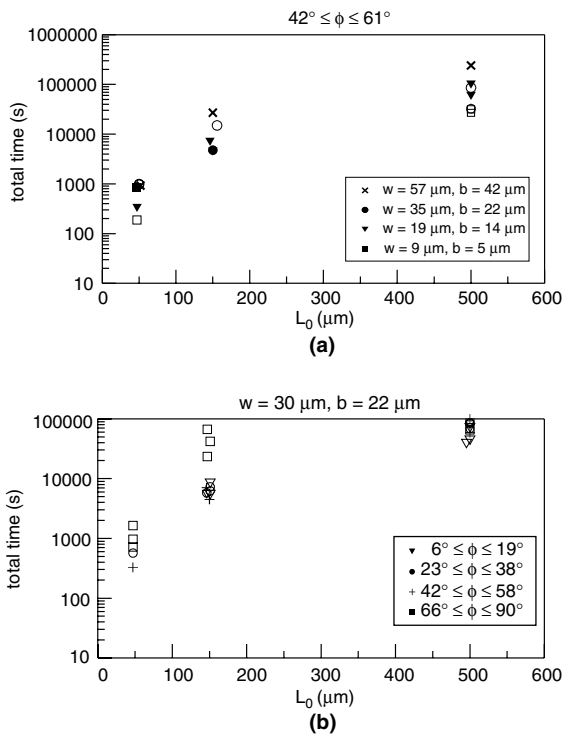


Fig. 11. Flooding time as a function of microchannel depth.

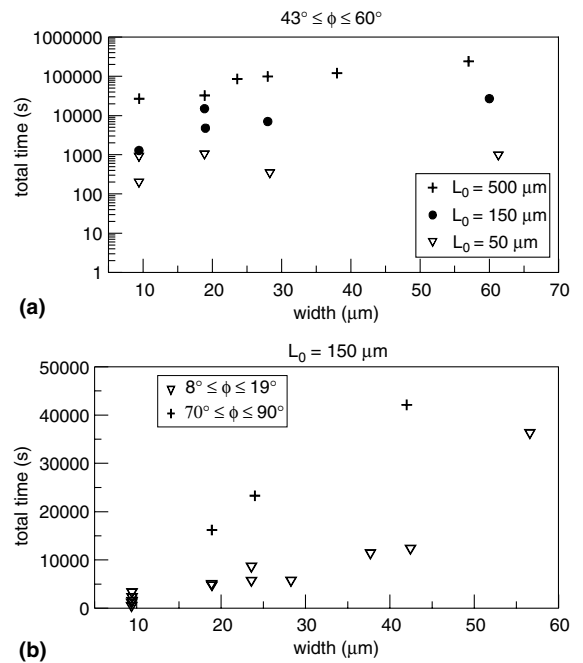


Fig. 12. Flooding time as a function of microchannel width.

6.1. Effect of microchannel depth (L_0)

As could be expected, for a given cross-section, deeper microchannels take longer to flood. This can be seen in Fig. 11(a) where the time, t , taken to flood a microchannel is plotted as a function of its depth. In general, it can be seen that the time to flood increases nonlinearly with depth, L_0 . For example, in Fig. 11(a), for $w = 57 \mu\text{m}$ and $b = 42 \mu\text{m}$, the flooding time increases rapidly from 1000 s to 30,000 s to 300,000 s as L_0 increases from 50 to 150 to 500 μm . Similar behavior is observed for micro-

channels of other sizes. Fig. 11(b) shows flooding time as a function of depth, for various contact angles and fixed w and b . Despite the scatter in the data, the nonlinear increase in time with L_0 can be clearly seen.

6.2. Effect of microchannel width (w) and breadth (b)

In almost all the experiments performed, the time taken to flood the microchannel increased slightly with increasing cross-sectional (w and b) area as shown in Fig. 12(a). For example, for $L_0 = 500 \mu\text{m}$, the time taken

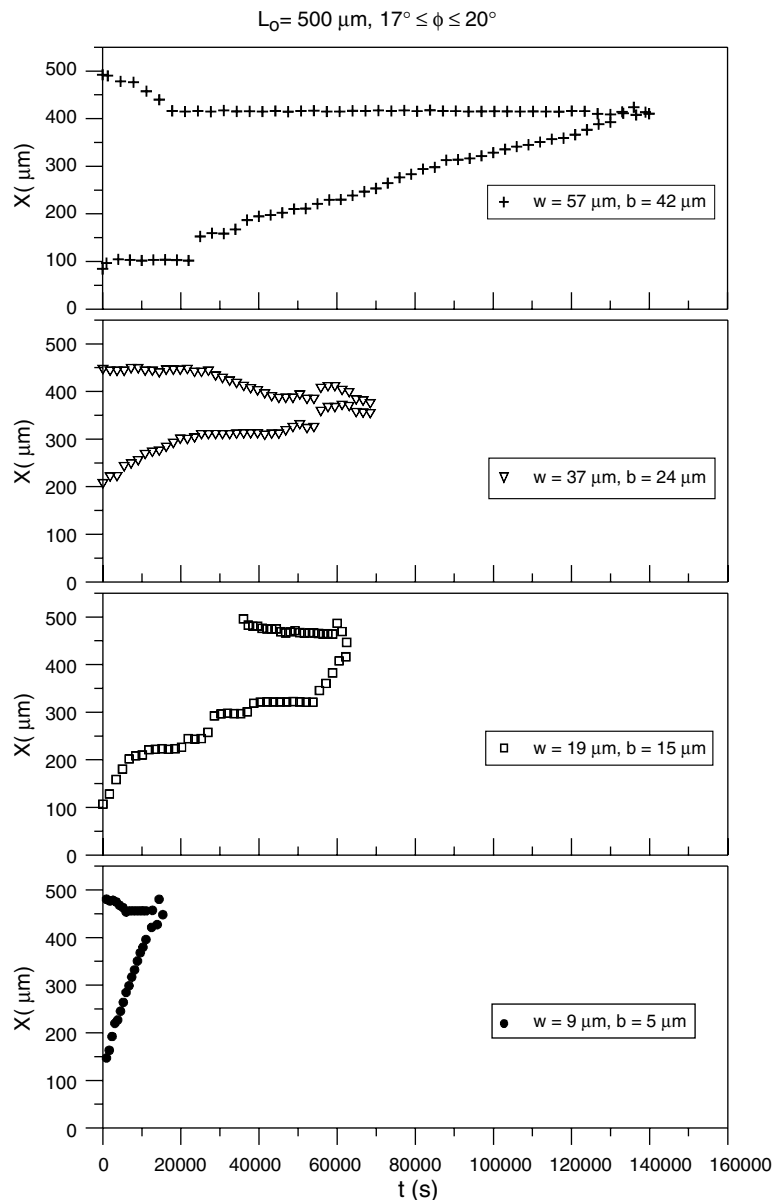


Fig. 13. Location of the water–air interface as a function of time for various microchannel widths and breadths ($L_0 = 500 \mu\text{m}$ and $17^\circ \leq \phi \leq 20^\circ$).

to fill the microchannel increases from 30,000 s to 200,000 s as the width increases from 9 to 56 μm . Fig. 12(b) shows the variation of filling time as a function of width, for $L_0 = 150 \mu\text{m}$. From Fig. 12(b) it is clear that for a given contact angle, the filling time increases with increasing width. The effect of the increase in the microchannel width and breadth can be further illustrated if one plots the location of the water–air interface (relative to the open end) as a function of time (Fig. 13 for $L_0 = 500 \mu\text{m}$ and $\phi \sim 20^\circ$). The increase in the flooding time with increase in microchannel cross-sectional area can be clearly seen in Fig. 13. Similar data were obtained for the 150 and 50 μm deep microchannels.

6.3. Effect of contact angle (ϕ)

The filling time is also affected by the contact angle. This is shown in Fig. 14(a). For example, for $w = 38 \mu\text{m}$ and $b = 24 \mu\text{m}$, the time taken to fill the microchannel increases from 38,000 s to 100,000 s as the contact angle increases from 8° to 58° . Fig. 14(b) shows the variation of the filling time with contact angle for a fixed $w = 9 \mu\text{m}$ and $L_0 = 50, 150, \text{ and } 500 \mu\text{m}$. For $L_0 = 500 \mu\text{m}$, the flooding time increases from 15,000 s to 30,000 s as the contact angle increases from 13° to 65° . From Fig. 14(a) and (b) it can be seen that, in general,

as the contact angle increases, the time taken to flood the microchannel also increases, for a given depth, mouth width and breadth.

Fig. 15 shows the location of the water–air interfaces as a function of time, for various contact angles ($L_0 = 500 \mu\text{m}$, $w = 9 \mu\text{m}$ and $b = 5 \mu\text{m}$). The increase in the flooding time with increase in contact angle is clearly seen in Fig. 15. Similar results are obtained for the shorter microchannels ($L_0 = 150$ and $50 \mu\text{m}$).

The increase in the contact angle also influences the time taken for the back interface to appear (Fig. 16(a)). From Fig. 16(a), it is clear that as the contact angle increases, the time taken for the back interface to appear also increases. For example, in Fig. 16(a), for $L_0 = 500 \mu\text{m}$, the time taken for the back interface to form increases from 30 s to 300,000 s as the contact angle increases from about 20° to about 68° .

The formation of a back interface at the closed end of the microchannels is due to a liquid film that flows along the corners of the channels. When this film has traveled from the initial position of the front interface and reaches the closed end of the microchannel it merges and forms the back interface. Quantitative measurement of this thin film was not possible in the setup used in the experiments; however an attempt was made to calculate the mean velocity of the thin film front. The mean velocity of the leading edge of the film in the corners was calculated by dividing the distance traveled from the initial position of the front interface (where the film starts) to the position where the back interface was formed by the time elapsed between these two events. The calculated mean velocity of the film along the corners as function of the contact angle is shown in Fig. 16(b). From the figure it can be seen that the higher the contact angle, the lower is the mean velocity of the leading edge of the film. The results shown in Fig. 16(b) constitute another way to assess the effect of the contact angle on the flooding time. As the contact angle increases, the mean film velocity decreases, which means that it will take longer for the back interface to appear and the microchannels will take longer to fill. The mean velocity of the leading edge of the thin film increases nonlinearly with contact angle. The observed behavior demonstrates the role played by surface forces in sucking liquid along the corners of the microchannels.

For a given width and contact angle, the large increase in flooding time with depth supports the fact that the time for which a boiling surface is exposed to the test liquid may be a parameter in determining the number of cavities that become active.

7. Model development

A simple one-dimensional model was developed to predict the movement of a single liquid–gas interface

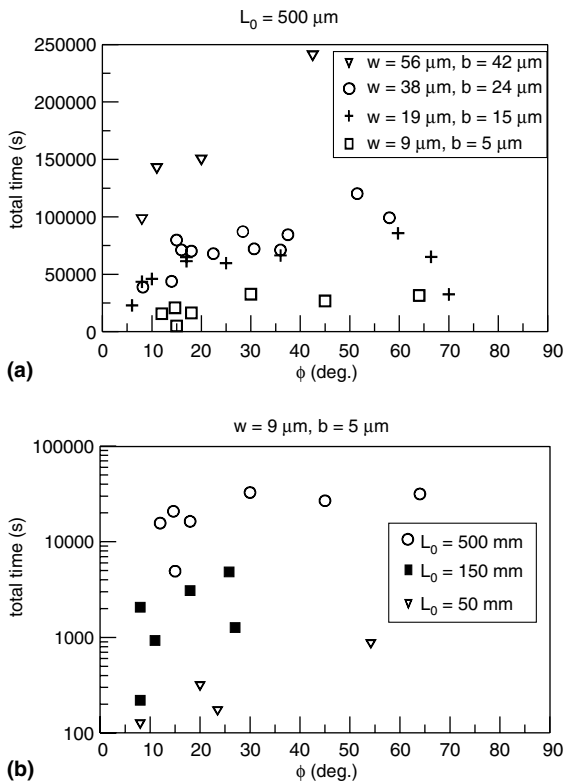


Fig. 14. Flooding time as a function of contact angle.

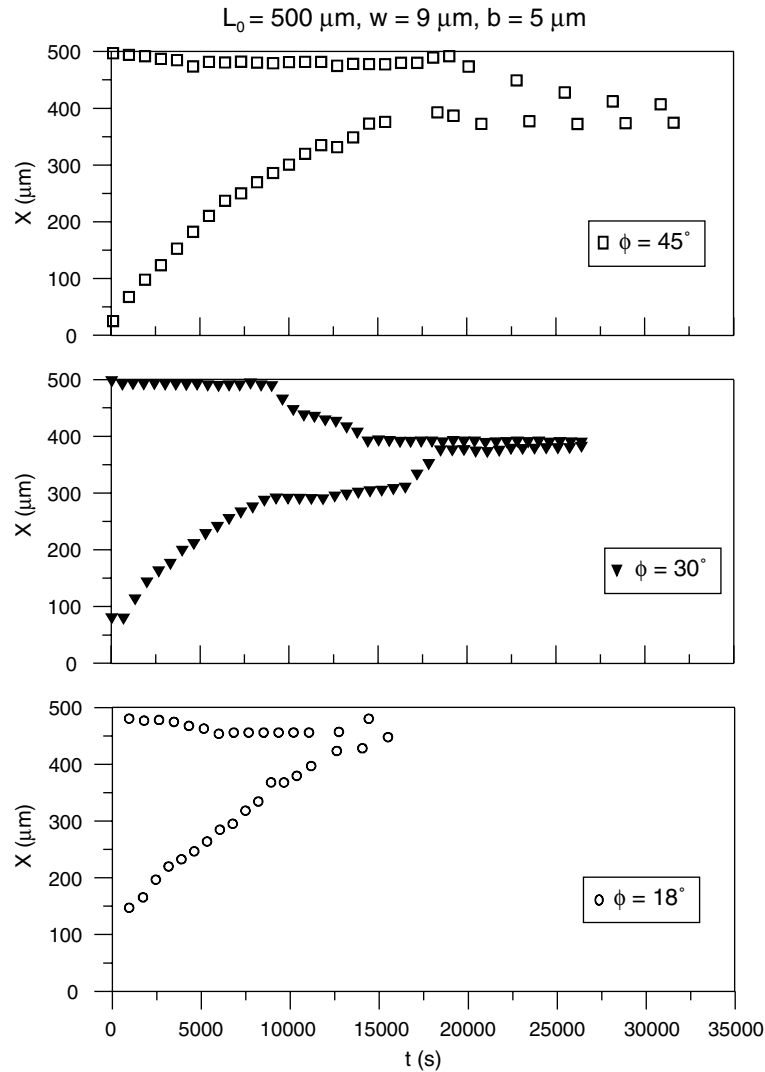


Fig. 15. Location of the water–air interface as a function of time for various contact angles ($L_0 = 500 \mu\text{m}$, $w = 9 \mu\text{m}$ and $b = 5 \mu\text{m}$).

as a result of gas diffusion. Fig. 17 shows details of the control volume. In this model, the liquid moving from the open end towards the closed end of the microchannel is assumed to represent a semi-infinite medium. Air is assumed to diffuse into the liquid, while the diffusion of the liquid into air is taken to be negligible. No evaporation is considered.

Assuming the air to be an ideal gas, the number of moles of air present in the microchannel at any given time can be written as,

$$\frac{P_{\text{air}} V_{\text{air}}(t)}{\mathfrak{R}T} = n_0 - \int_0^t J_{1,u} dA_{\text{int}} dt \quad (2)$$

where P_{air} is the pressure of the air, V_{air} is the volume of air at any time t , A_{int} is the surface area of the liquid–air

interface, \mathfrak{R} is the universal gas constant, T is the temperature, n_0 is the initial number of moles of air given by $\frac{P_0 L_0 w b}{\mathfrak{R}T}$, P_0 is the atmospheric pressure, L_0 is the depth of the channel, w is the width and b is the breadth. In Eq. (2) the integral represents the total number of moles of air diffused into water during the time t , through the front interface.

The molar flux, $J_{1,u}$, of air diffusing into water (considered to be a semi-infinite medium) through the front interface is given by,

$$J_{1,u} = c_{\text{mix}} \sqrt{\frac{D_{12}}{\pi \cdot t}} (x_{1,u} - x_{1,0}) \quad (3)$$

where $c_{\text{mix}} = \rho/M$ in kmol/m^3 (ρ is density and M is the molecular weight) is the molar concentration of the

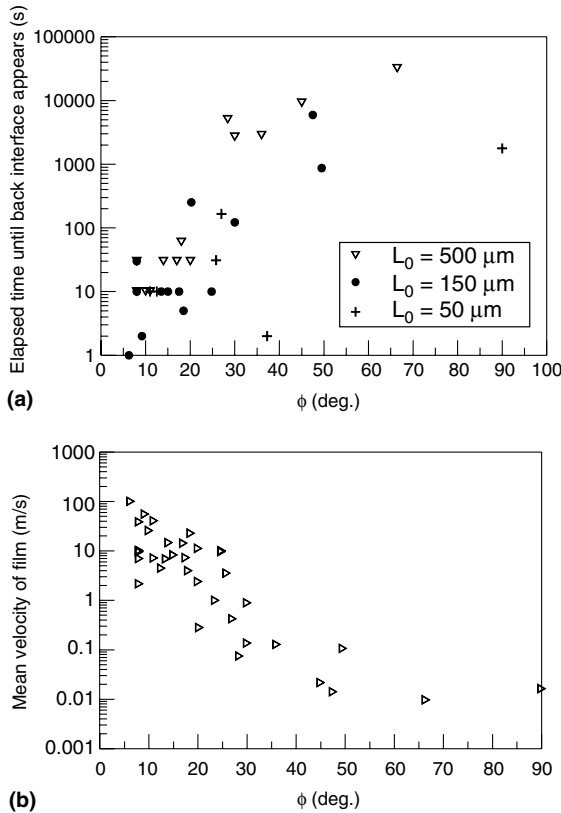


Fig. 16. (a) Time taken for the back interface to appear and (b) mean velocity of film in the corners as a function of the contact angle.

water–air mixture, D_{12} is the diffusion coefficient, $x_{1,u}$ and $x_{1,0}$ are the mole fractions of air at the interface and the initial mole fraction of air in the liquid, respectively. The pressure in the air is taken as the liquid pressure plus the capillary pressure, i.e.,

$$P_{\text{air}} = P_{\text{liq}} + \frac{\sigma}{R}, \quad \frac{1}{R} = \left(\frac{1}{R_1} + \frac{1}{R_2} \right) = \frac{2(w+b)\cos\phi}{w \cdot b} \quad (4)$$

It is assumed that the initial concentration of air in water ($x_{1,0}$) is zero, (i.e., $x_{1,0} = 0$) and that there is no liquid present in the air. Hence the concentration of air, $x_{1,s} = 1$.

The mole fraction of air at the interface ($x_{1,u}$) can be calculated as $x_{1,u} = \frac{x_{1,s}}{He} = \frac{1}{He}$, where He is the Henry number calculated as $He = \frac{C_{He}}{P_0}$, and C_{He} is the Henry constant in Pa. Using the numerical values for properties of water and air given by Mills [15], D_{12} was calculated to be $2.77 \times 10^{-9} \text{ m}^2/\text{s}$.

Substituting Eqs. (3) and (4) into Eq. (2) and integrating from time 0 to t yields,

$$\frac{P_{\text{air}} V_{\text{air}}(t)}{\mathcal{R}T} = \frac{P_0 L_0 w b}{\mathcal{R}T} - 2c_{\text{mix}} \frac{P_0}{C_{He}} A_{\text{int}} \sqrt{\frac{D_{12} t}{\pi}} \quad (5)$$

The volume of air in the microchannel at time t is given by,

$$V_{\text{air}}(t) = [wb(L_0 - X(t)) + V_{\text{cap}}] \quad (6)$$

where the first term represents the volume of air in the rectangular portion ($X(t)$ is the position of the interface) and V_{cap} represents the volume of air in the curved cap shaped portion. Since an exact calculation of V_{cap} and A_{int} for the rectangular geometry of the microchannel is extremely difficult (the shape of the interface is such that the surface energy is minimum), we use an approximation. In this approximation we assume the microchannel to be circular in cross-section, with the cross-sectional area of the circular microchannel equal to wb (cross-sectional area of the rectangular microchannel). Now, for a given contact angle, we can determine both V_{cap} and A_{int} . The resulting equations for A_{int} and V_{cap} are given as,

$$A_{\text{int}} = \pi r_{\text{eq}}^2 \left[1 + \left\{ \frac{(1 - \sin(\phi))}{\cos(\phi)} \right\}^2 \right],$$

$$V_{\text{cap}} = \frac{\pi}{6} r_{\text{eq}}^3 \left[3 \left\{ \frac{(1 - \sin(\phi))}{\cos(\phi)} \right\} + \left\{ \frac{(1 - \sin(\phi))}{\cos(\phi)} \right\}^3 \right] \quad (7)$$

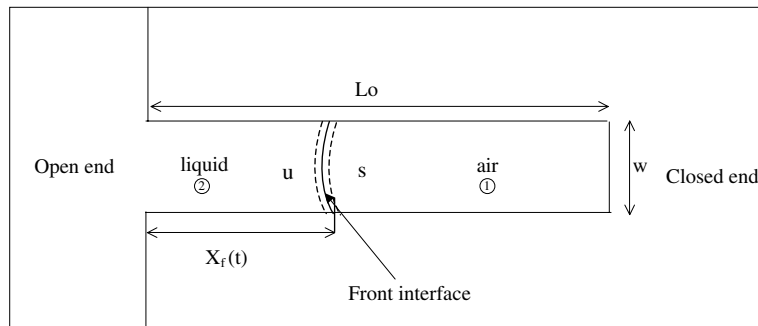


Fig. 17. Control volume for the model.

where r_{eq} is the equivalent radius of the circular micro-channel ($r_{\text{eq}} = (wb/\pi)^{0.5}$). Substituting Eqs. (6) and (7) into Eq. (5) and solving for $X(t)$ yields,

$$X(t) = L_0 \left(1 - \frac{P_0}{P_{\text{air}}} \right) + \frac{V_{\text{cap}}}{wb} + 2c_{\text{mix}} \frac{\Re T}{C_{\text{He}}} \frac{P_0}{P_{\text{air}}} \frac{A_{\text{int}}}{wb} \sqrt{\frac{D_{12}t}{\pi}} \quad (8)$$

Eq. (8) is used to predict the position of the single interface as a function of time. The first experimental data

point was used as the initial position (at $t = 0$) for $X(t)$ in the model.

Fig. 18(a) shows a comparison of the experimental data and the model predictions for varying cross-sectional area while Fig. 18(b) shows the comparison for various contact angles. From Fig. 18 it can be seen that there is qualitative agreement between the experimental data and the model predictions. The step change in the interface location observed in the experiments may be due to the liquid flow in the corners of the microchannel.

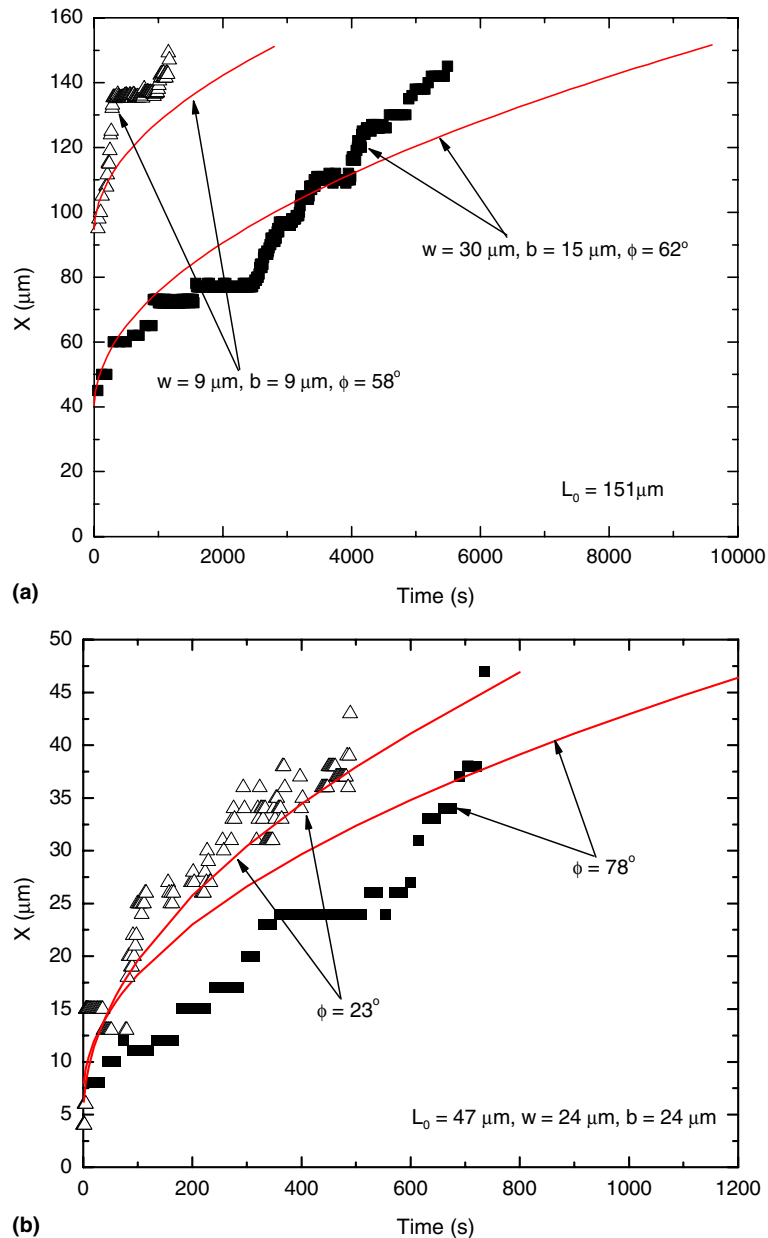


Fig. 18. Comparison of experimental data and model predictions (a) effect of varying w and b and (b) effect of varying contact angle.

However, in general, the model predicts much longer filling times than those observed in the experiments. We believe that this is due to the fact that the liquid is sucked into the microchannel along the corners as a thin film; this phenomenon is not accounted for in the model. The model appears to capture the effects of changing w , b , and ϕ on the interface location fairly well. For given L_0 and ϕ , decreasing w and b results in a decrease

in the filling time. Similarly, for given L_0 , w and b , decreasing ϕ results in a decrease the filling time.

The same analysis of the single interface was then applied to predict the location of the front interface for low contact angles cases (when two interfaces are present). A comparison of the experimental data with analytical results, for the front interface, is shown in Fig. 19(a) and (b). It must be noted that, in this case, the capillary

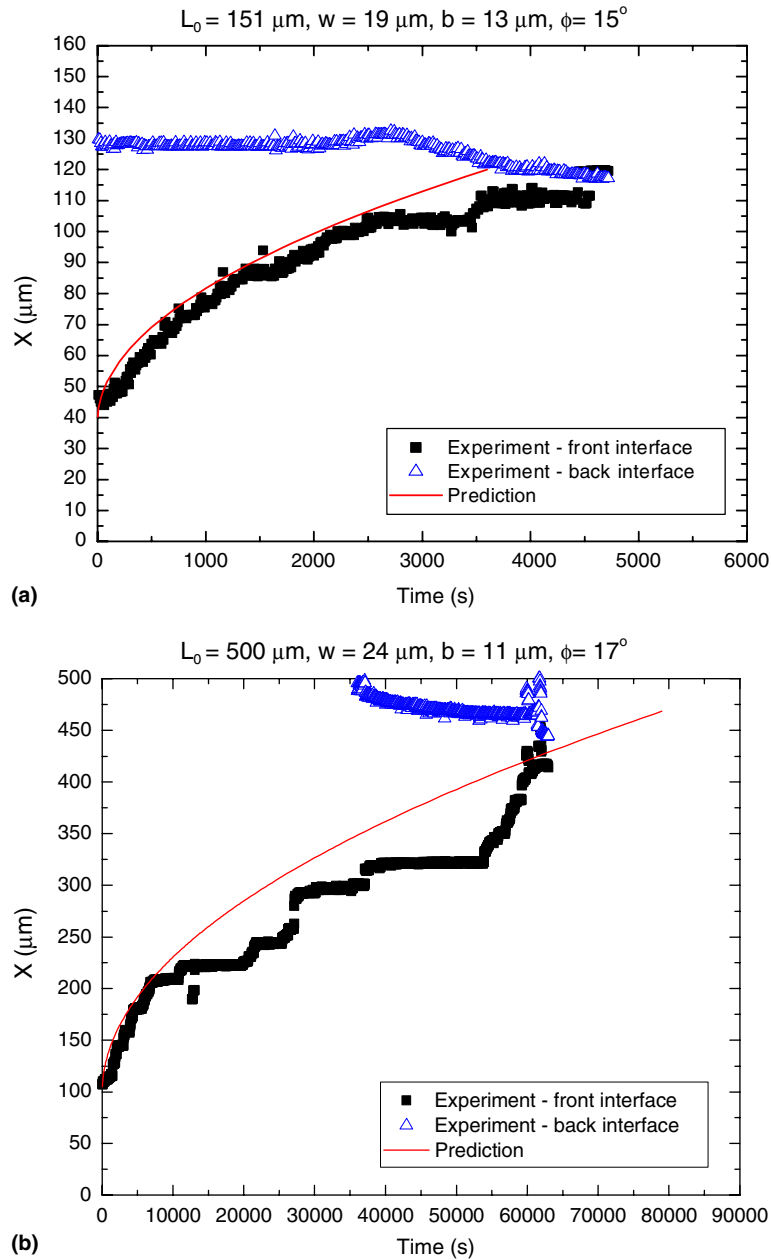


Fig. 19. Comparison of experimental data and model predictions for low contact angles.

pressure is multiplied by two because of the presence of the back interface. From Fig. 19 it can be seen that though the predicted position of the front interface as a function of time does not deviate much from that observed in the experiments.

The formation and growth of the liquid column at the closed end of the microchannels may be explained by the thin film liquid flow along the walls. Since the present experiments did not provide enough information, the details of the thin film cannot be discussed in this work. Migun et al. [16,17] proposed a model for film flow in a dead-end conic capillary. In their model, the radius of curvature of the film naturally varied along the length of the conic channel, which provides the driving potential for the film flow. They found that the growth of the back interface was proportional to the cubic root of time. However, their model cannot be applied to the present geometry since there is no change in the cross-sectional area of the channel.

8. Summary

Experiments were conducted to investigate the gas/vapor entrapment process in closed-end microchannels of various sizes. These closed-end microchannels represented cylindrical cavities (mouth angle of 90°) on a heater surface that may become active nucleation sites during boiling, provided the liquid entraps gas/vapor inside. The contact angle between the test fluid (DI water) and the silicon microchannel was also varied using different surface cleaning procedures. The effect of the diffusion of the gas into the liquid has also been investigated.

In all the experiments performed, the microchannels were completely filled, given sufficient time (minutes to hours to days). The cavity mouth angles were about 90° , while the contact angles measured were less than 90° . Hence the condition for gas entrapment given by Eq. (1) was not met. Two or more interfaces connected by a thin liquid film were observed for low contact angles ($\phi \leq 50^\circ$). For $\phi > 50^\circ$, only one interface was observed. Occasionally, for $\phi \leq 15^\circ$, three interfaces were observed. In the range of parameters considered, the dimensions of the microchannels did not affect the number of interfaces observed. In general,

- (i) For fixed width, breadth and contact angle, the flooding time increases nonlinearly (up to two orders of magnitude) with increasing microchannel depth (L_0).
- (ii) For fixed depth and contact angle, the flooding time increases with increasing microchannel width (w) and breadth (b).
- (iii) For fixed depth, width and breadth, the flooding time increases with increasing contact angle (ϕ).

The most pronounced effect on the flooding time was the change in the microchannel depth, followed by the effect of the microchannel width and breadth and last, though still important, the effect of the variation of the contact angle.

A simple one-dimensional mass diffusion model for a semi-infinite medium shows reasonable agreement for the cases with only one interface. The model accounts for the effects of varying w , b and ϕ on the movement of the interface. However, this model cannot explain the appearance and movement of the back interface. The movement of the back interface may be explained by the liquid film flow along the corners of the rectangular microchannels, but the investigation of the details of this flow was beyond the scope of this work.

Acknowledgement

This work received support from NASA under the Fluid Physics Program.

References

- [1] S.B. Bankoff, Entrapment of gas in the spreading of a liquid over a rough surface, *AICHE J.* 4 (1958) 24–26.
- [2] C.H. Wang, V.K. Dhir, Effect of surface wettability on active nucleation site density during pool boiling of water on a vertical surface, *J. Heat Transfer* 115 (1993) 659–669.
- [3] C.H. Wang, V.K. Dhir, On the gas entrapment and nucleation site density during pool boiling of saturated water, *J. Heat Transfer* 115 (1993) 670–679.
- [4] G.R. Warriar, unpublished notes, 2002.
- [5] V.P. Carey, *Liquid–Vapor Phase-change Phenomena*, Taylor & Francis, Bristol, Pennsylvania, 1992.
- [6] E.W. Washburn, The dynamics of capillary flow, *Phys. Rev.* 17 (1921) 273.
- [7] J.L. Poiseuille, *Mém. de Savans étrangers* 9 (1846) 433.
- [8] J. Szekely, A.W. Neuman, Y.K. Chuang, The rate of capillary penetration and the applicability of the washburn equation, *J. Coll. Interf. Sci.* 35 (1971) 273–278.
- [9] L.J. Yang, T.J. Yao, Y.L. Huang, Y. Xu, Y.C. Tai, Marching velocity of capillary menisci in microchannels, in: 15th IEEE International Conference (MEMS '02), Las Vegas, USA, 2002.
- [10] G.A. Akselrud, M.A. Altshuler, *Introduction to Capillary-Chemical Technology*, Khimia, Moscow, 1983.
- [11] G.I. Dovgyallo, N.P. Migun, P.P. Prokhorenko, The complete filling of dead-end conical capillaries with liquid, *J. Eng. Phys.* 56 (4) (1989) 395–397.
- [12] C.H. Wang, unpublished notes, 1993.
- [13] N.P. Migun, M.A. Azuni, Filling of one-side-closed capillaries immersed in liquids, *J. Coll. Interf. Sci.* 181 (1996) 337–340.
- [14] A.V. Pesse, Experimental study of the gas entrapment process in closed-end microchannels, MS thesis, University of California–Los Angeles, Los Angeles, 2004.
- [15] A.F. Mills, *Basic Heat and Mass Transfer*, Prentice Hall, Upper Saddle River, New Jersey, 1999.

- [16] N.P. Migun, A.I. Shnip, L.E. Reut, Role of the diffusion mechanism of mass transfer processes in conic capillaries submerged in a liquid, *J. Eng. Phys. Thermophys.* 75 (6) (2002) 1412–1421.
- [17] N.P. Migun, A.I. Shnip, Model of film flow in a dead-end conic capillary, *J. Eng. Phys. Thermophys.* 75 (6) (2002) 1422–1428.